Unraveling the Formation Process of an Organic Photovoltaic Active Layer during High-Speed Coating *via* a Synergistic Concentration-Temperature Gradient Control Strategy

Bo Xiao[1], Weiwei Wu[1], Shanshan Wang[1], Ji Wan[1], Yiming Shao[1], Rui Sun[1, 2, 3*], Jie Min[1*]

[1]The Institute for Advanced Studies, Wuhan University, Wuhan 430072, China

E-mail: sun.rui@whu.edu.cn; min.jie@whu.edu.cn

[2]Institute of Polymer Optoelectronic Materials and Devices, State Key Laboratory of Luminescent Materials and Devices, South China University of Technology, Guangzhou 510640, China

[3]Key Laboratory of Advanced Electrode Materials for Novel Solar Cells for Petroleum and Chemical Industry of China, School of Chemistry and Life Sciences, Suzhou University of Science and Technology, Suzhou 215009, China

Abstract

The Layer-by-Layer (LbL) strategy has emerged as a highly effective approach for enhancing the performance of organic photovoltaics (OPVs), notably boosting light harvesting and fill factor through spectral complementarity and morphology optimization. Crucially, the LbL processing strategy has been found to mitigate or overcome the decline in power conversion efficiency (PCE) during high-speed blade coating. Despite these advancements, there remains a scarcity of research into the film-formation process and the corresponding control strategies in high-speed printing. A novel synergistic concentration-temperature gradient control (SCTGC) strategy aimed at achieving high-performance LbL-type active layers at ultra-fast coating speeds. Our investigation reveals that both baseplate temperature and solution concentration exert a nonmonotonic regulatory influence on PCEs. Fine-tuning the concentration gradient proves instrumental in balancing microfluidic competition within the wet film, thereby facilitating stable mass transport during the film formation process, and enhancing the high-speed processability of the relevant OPV system. Additionally, the variations in crystallization kinetics under different temperatures were monitored. This work sheds light on the coating mechanism and film formation in high-speed coating, highlighting the efficiency of the SCTGC method.

Introduction

Over the past few decades, organic photovoltaics (OPVs) have garnered significant attention from the academic and industrial communities as a promising avenue for harnessing renewable solar energy. Note their versatility, lightweight, affordability, cost-effectiveness, and printability—all of which add to their attractiveness in a range of applications—are what are driving this interest.[1-6] By utilizing narrow bandgap small molecule non-fullerene acceptors (SM-NFAs), fine-tuning their molecular structures, and applying state-of-the-art fabrication techniques, it is possible to deliver promising power conversion efficiencies (PCEs) of more than 20%.[7-12] Simultaneously, considerable efforts have been focused on addressing the stability challenges inherent in OPVs.[13-15] Although the field of OPVs has achieved significant progress in terms of efficiency, stability, and cost, concerns regarding fabrication scalability are becoming more prevalent.[16, 17] As such, a major obstacle to commercial applications is how to shift from lab-scale manufacture of OPV devices to high-throughput large-scale fabrication *via* using promising morphology control strategies.

The challenges facing morphology control of large-scale OPV fabrication generally encompass the selection of eco-friendly solvents, the utilization of large-area printing technologies, and ensuring compatibility with high-throughput processes.[3,18] Tremendous research efforts have been devoted to modifying bulk-heterojunction (BHJ) microstructure at multi-scales, and a range of morphological modification and processing condition optimization approaches were developed. Nevertheless, rational BHJ microstructure optimization conducted by donor: acceptor (D: A) mixed solutions remains challenging, in terms of the high-throughput or high-speed processing techniques (like doctor-blade (DB) coating and slot-die (SD) coating),[17, 19-22] normally leads to poor BHJ blend microstructure and worse device photovoltaic performance. In particular from a morphological perspective, the emerging sequential deposition or layer-by-layer (LbL) fabrication of donor/acceptor (D/A) materials, regarded as the most important advancement of morphology control in recent years, brings great

opportunities.[23, 24] Numerous studies have shown that the LbL-processed method can lead to the formation of an ideal vertical phase, the improvement of light harvesting and charge transport properties, and thus effectively improve device efficiency and morphological stability of relevant OPV systems, as compared to the D:A mixing-processed BHJ active layers.[25-30] Moreover, our previous work demonstrated that the LbL-printing technique can effectively overcome the scaling lag of solar module efficiency[31] and significantly facilitate high-speed (> 30 m min^{-1}) fabrication of OPV systems without device performance losses.[22] All these results indicate that the LbL coating approach is a promising strategy to effectively reduce the efficiency-stability-cost gap of OPV systems and even a superior alternative to the BHJ-processing method for the high-speed production of large-scale OPV devices. Of particular note is that a techno-economic analysis suggests that a high-speed coating can significantly reduce the minimum sustainable price of module manufacturing.[22, 32] Therefore, in-depth investigations on the key factors influencing the film formation of active layer morphology fabricated by LbL-printing technologies, which are compatible with high-throughput or high-speed processes, are strongly needed.

The difference in PCEs between low-speed and high-speed DB- and SC-printing devices based on both BHJ and LbL architectures inevitably brings great challenges, mainly attributed to three aspects. First, there are differences in the regimes of fluid mechanical deposition. The Landau-Levich regime eventually replaces the evaporative regime in the deposition regimes as the coating speed rises. During the film formation process, adhesive force and surface tension eventually take center stage in determining the quality of morphology control.[21] Second, there is a variation in the driving force for film formation. At low coating speeds, film formation relies on the external shear force sheet transmitted from the meniscus blade; the flattened wet film crystallizes instantaneously after passing through the three-phase line, guaranteeing the uniformity of the film. While in the high-speed coating, the intrinsic microfluidics in the wet film, rather than the strong blade-meniscus, guide the film formation process.[21, 33, 34] Thus, the material system with poor spontaneous film-forming capacity is exposing its

disadvantage in the high-speed coating.[22, 35] Finally, the change of the Landau-Levich regime in solution properties always results in a thick film, in contrast, the diluted solution can be used to keep the film thickness of around 100 nm.[8, 36, 37] Nevertheless, this is still a lack of consensus on how to deal with the abovementioned challenges. Moreover, the underlying film-formation mechanisms are also not yet clearly understood, because moving from lab-scale spin-coating to large-scale manufacturing processes involves many parameter changes,[21, 38, 39] including processing solvents, coating techniques, coating speed, device scale, environmental conditions, printing substrates, *etc*. Thus, to effectively find OPV systems with high coating-speed tolerance, rationally control the microstructure of D/A blends and quickly facilitate the applications of scalable high-throughput techniques in solution processed large-scale industrial manufacturing of thin-film organic electronics, developing effective morphology control strategies to overcome the performance variations as well as fully understanding the intrinsic microfluidics-guided film formation process and lateral morphology evolution are essential prerequisites.

In this work, a high-efficiency OPV system based on the commercially available materials, PM6 (serving as the donor) and BTP-eC9 (acting as the acceptor), was chosen as the model system (**Figure 1A**). Its morphology control becomes a crucial step in the transition from lab-scale spin-coating to large-scale high-throughput manufacturing processes. We found that the LbL-processed PM6:BTP-eC9 active layer morphologies fabricated by different DB-coating speeds not only possess varied degrees of phase separation characteristics in blends but also present different aggregation kinetics during the DB-coating process. Furthermore, we demonstrate that the LbL-processed morphologies fabricated by high coating speeds could be effectively changed to suitable phase separation by synergistically regulating the print solution concentration and baseplate temperature. Moreover, the universality of this novel synergistic concentration-temperature gradient control (SCTGC) strategy was demonstrated by introducing various processing solvents. In particular, the counterbalancing effect of concentration gradients in microscopic hydrodynamics and

the regulatory influence of substrate temperature on the dissolution-reaggregation process were unraveled.

Results and Discussion

In the previous work, we systematically investigated the BHJ- and LbL-processing strategies *via* the DB-coating technology and evaluated multiple target parameters, including device efficiency, operational stability, physical kinetics, and morphological characteristics.[40] Recently, the device efficiency and stability improvements of developed binary and ternary OPV systems as well as the newly designed systems rely heavily on the LbL-processing approach.[41-45] **Figure 1B** further depicts the LbL processing strategy based on the DB-coating technology, which was employed in the potential investigation of high-speed manufacturing compatibility. Both PM6 and BTP-eC9 layers were fabricated under a coating speed of 6.0 m min^{-1} for simulating the high-speed situation, which led to a distinctive film formation process from the low coating speeds (0.8-1.2 m min^{-1}) reported previously.[46, 47] As shown in (**Figure 1C**, the effects of the blade-coating speeds of BTP-eC9 on the crystallization processes and film-formation behaviors in chloroform (CF) are obvious, supported by the color mapping investigations of *in-situ* ultraviolet-visible (UV-Vis) absorption spectra of PM6/BTP-eC9 blends.

In particular, the whole film-formation process can be divided into three different stages based on *in-situ* absorption intensities for the low and high-speed coated blends (**Figure 1D**): (1) quick solvent evaporation; (2) crystalline growth; and (3) film formation.[17, 46, 48, 49] Compared with the PM6/BTP-eC9 blend fabricated at a low speed of 1.2 m min^{-1}, we observed notable differences in stages (including I, II, and III) in the LbL blend fabricated by a high speed of 6.0 m min^{-1}. The quick solvent evaporation process (stage I) and crystalline growth process (stage II) in the high-speed coated blend showed longer times than that of the low-speed coated blend. In particular, this extended solvent evaporation and molecular organization processes lead to low crystallization of BTP-eC9, supported by the UV-Vis spectroscopy measurements (**Figure S1**). The film-

coated at a low speed exhibits a more red-shifted spectrum, as compared to the high-speed coated blend, indicating more obvious acceptor molecular aggregations in the solid state. As presented in **Figure 1E**, the atomic force microscopy (AFM) image of the low-speed coated blend exhibits more pronounced phase separation with larger domain sizes, confirming its bi-continuous network structures. In contrast, the AFM image of the high-speed coated blend shows uniform but unclear phase separation with a low root-mean-square (RMS) value of 1.61 nm. Especially, the higher RMS value (5.04 nm) of the low-speed coated blend than that of the high-speed coated blend can be observed from the AFM image, which is beneficial to charge transport and charge extraction properties.[50, 51] As a result, these differences in film-formation behaviors and morphological characteristics reflect the statistical photovoltaic metrics and PCE histogram obtained from the two blends fabricated by low- and high-coating speeds (**Figure 1F**). Based on all the results discussed above, we concluded that the conventional processing conditions can not obtain the favorable blend morphology and device performance at high coating speed. Thus, it is urgent and necessary to find promising processing strategies to modulate the bulk microstructure of the active layer under high-speed coating and expand the processing window of the active layer system. In response to the abovementioned dilemma and requirements, here we have developed an effective approach to overcome or eliminate the PCE gaps of relevant devices based on low- and high-speed coated blends, that is, to synergistically fine-tune the substrate temperature and solution concentration (named a SCTGC approach as mentioned above). The choice of the coating temperature is primarily based on the boiling point of the solvent, while the selection of the solution concentration mainly revolves around achieving the most suitable film thickness. What's more, according to the specific solution concentration, temperature regulation can prolong or shorten the film formation time, so that the acceptor and donor materials can be orderly and reasonably precipitated in the wet film, forming a suitable blend morphology.

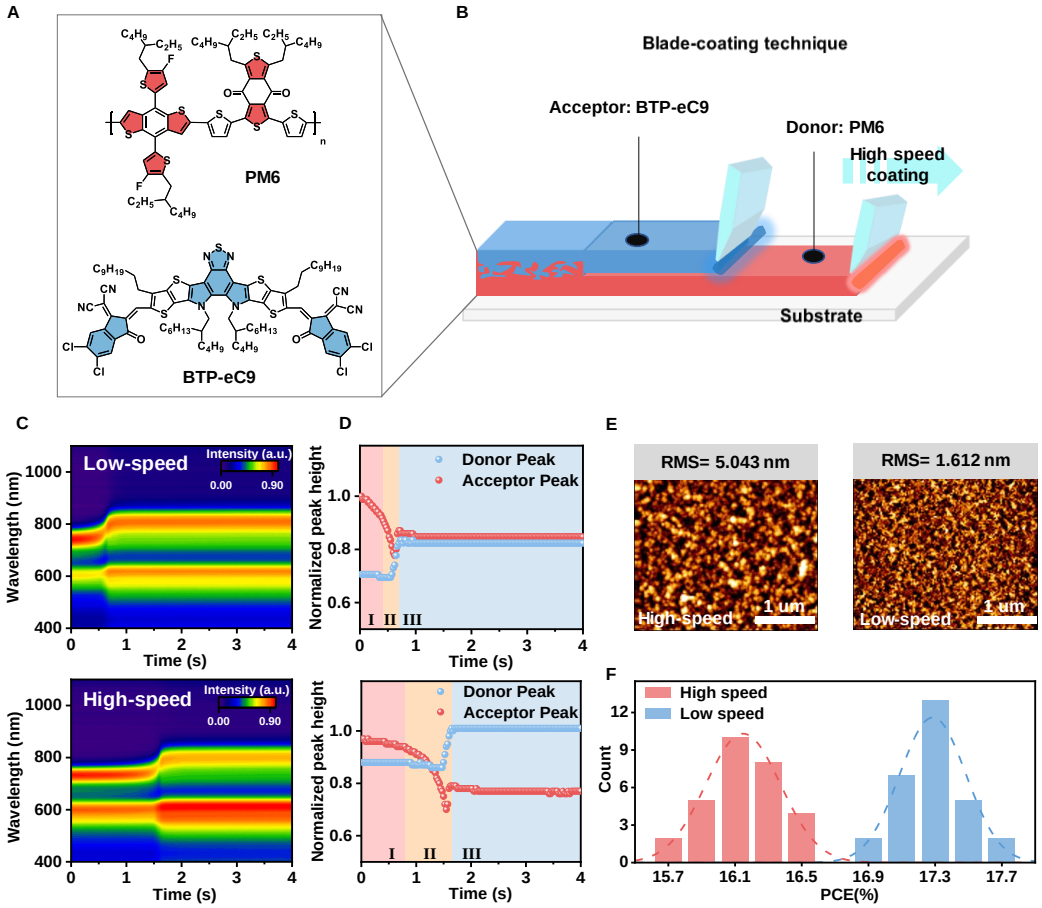

Figure 1. (A) The molecular structures of PM6 and BTP-eC9. (B) Schematic illustration of the LbL blade-coating approach. (C) The color mapping of *in-situ* UV-vis absorption spectra of PM6/BTP-eC9 (CF) evolution from the solution (0 s) to the film (4 s), fabricated by low-speed and high-speed, respectively (left). The color scale bar represents the absorption intensities. (D) The corresponding changes in the integrated *in-situ* UV-vis absorption intensities for PM6 and BTP-eC9: quick solvent evaporation stage (pink area) (I), crystal growth stage (bright yellow area) (II), and film formation stage (brilliant blue area) (III). (E) AFM height images (3×3 μm^2) of the LbL-processed PM6/BTP-eC9 blends fabricated at low and high speeds, respectively. (F) Histograms of the PCE counts for 25 individual PM6/BTP-eC9 devices fabricated at low- and high-coating speeds.

The current density-voltage (*J*-*V*) curves of relevant high-speed coated LbL devices fabricated at different baseplate temperatures (from 28 to 58 °C) and various solution concentrations (from 4.6 to 7.6 mg mL^{-1}) measured under the illumination of an AM 1.5G solar simulator at 100 mW cm^{-2} were exhibited in the **Figure S2**, and the corresponding photovoltaic parameters are summarized in **Table S1**. As presented in **Figure 2A**, the PM6/BTP-eC9 LbL devices fabricated at high coating speeds display

dramatic changes in device performance from 11.70% to 17.74% PCE due to the synergetic variations of substrate temperature and solution concentration. Here we significantly investigated the effect of various solution concentrations on the photovoltaic performance of the high-speed coated blends fabricated at an optimal baseplate temperature (38 °C), as shown in **Figure 2B**. Solution concentration has exhibited a nonmonotonic regulation effect on the device efficiencies, especially in terms of the short circuit current density (J_{SC}) and fill factor (FF) values (**Table S1**). The relevant external quantum efficiency (EQE) spectra were provided in **Figure S3** and the calculated J_{SC} values are in good agreement with those measured from the *J-V* curves.[13] Consequently, the high-speed coated blend fabricated with a solution concentration of 6.1 mg mL^{-1} under the baseplate temperature of 38 °C shows the best PCE of 17.74 % (V_{OC} = 0.838 V, J_{SC} = 27.79 mA cm^{-2}, FF = 76.23 %). It is worth noting that this value is comparable to the device efficiencies of the LbL blends prepared at low coating speeds (**Figure 1F**), underscoring the effectiveness of this SCTGC approach.

To get a deep understanding of the physical dynamics in devices based on the high-speed coated blends prepared with various concentrations, we first investigated the exciton dissociation and charge generation properties *via* the photoluminescence (PL) measurements (**Figure S4**). Although similarly strong quenching of PL intensity can be measured in all the blends formatted from solution, higher quenching efficiency can be found in the blend fabricated with a solution concentration of 6.1 mg mL^{-1}, indicating more exciton dissociation property.[52] However, the lower (4.6 mg mL^{-1}) and higher (7.6 mg mL^{-1}) concentration solutions for constructing the high-speed coated LbL blends get a weaker quenching, which may result from the poor morphology of the relevant blends. Additionally, the photogenerated current density (J_{ph}) versus effective voltage (V_{eff}) was measured to calculate the exciton dissociation probabilities (P(E, T)=J_{ph}/J_{sat}, where J_{sat} is the saturation current density) to depict the exciton behavior (**Figure S5**).[53] The J_{ph}/J_{sat} value of the device with the best solution concentration gradient was 95.9%, while the J_{ph}/J_{sat} values of the devices prepared with dilute (4.6 mg mL^{-1}) and

concentrated (7.6 mg mL^{-1}) solutions were 91.4% and 94.4%, respectively,[54] which might be contributed to the dominance from film thickness (**Table S2**) and blend morphology as described below.

To further investigate the charge transport properties, we employed the space-charge-limited current (SCLC) method to analyze the charge-carrier mobility in these blends (**Figures S6-S7**). As shown in **Figure S8**, the hole and electron mobilities of the PM6/BTP-eC9 LbL devices based on the blend fabricated with a solution concentration of 6.1 mg mL^{-1} are 5.42×10^{-4} and 6.48×10^{-4} $cm^2\ V^{-1}\ s^{-1}$, respectively, which are much higher than those of the active layers fabricated with dilute (4.6 mg mL^{-1}) and concentrated (7.6 mg mL^{-1}) solutions. Moreover, to realize the charge recombination mechanisms, the *J-V* curve characteristics as a function of light intensity (P_{light}) were carried out, and the detailed analysis can be found in **Figures S9** and **S10**, respectively. Relevant results indicate that the optimal blend fabricated with a solution concentration of 6.1 mg mL^{-1} as compared to the other two blends displays less trap-assisted recombination loss in devices, also supported by the transient photovoltage (TPV) and transient photocurrent (TPC) measurements (**Figure S11**). Among these devices based on the high-speed coated blends, the device fabricated at optimal concentration gradient exhibits the longest TPV decay signal lifetime and shortest charge extraction time, demonstrating suppressed non-geminate recombination loss and efficient carrier extraction pathway.[13]

In our previous works,[23, 55] the rate of solvent evaporation and the vertical composition gradients of active layers can be effectively modulated by adjusting the baseplate temperatures (or ITO-substrate temperatures). Here we further found that the solution concentration of the top layer can not only be employed to fine-tune the blend microstructure but also significantly improve the high throughput processing property of the active layer system (**Figure 2B**). Considering that the concentration gradient-driven film formation processing mostly affects the morphology of the active layer, the grazing incidence wide-angle X-ray scattering (GIWAXS) and AFM measurements

were conducted to investigate the blend morphology and molecular packing behaviors. The two-dimensional scattering patterns of the abovementioned blends in the out-of-plane (OOP) and in-plane (IP) directions and the OOP and IP profiles acquired at the critical incident angle of 0.13° were shown in **Figure 2C** and **Figure S12**, respectively. Furthermore, the extracted parameters (the stacking distance and coherence length) of π–π (010) stacking and lamellar (100) peak are summarized in **Figure 2D** and **Table S3**. All the LbL blends exhibited obvious π-π stacking peaks at $q \approx 1.535$ Å^{-1} in the OOP direction, suggesting a prominent face-on orientation in blend films. The difference among lamellar (100) peaks of various blends is negligible. To research the crystallinity, the crystal coherence length (CCL) values of molecular packing were calculated by the Scherrer equation (Figure 2D), and the CCLs reached the highest value when the active layer film fabricated with a solution concentration of 6.1 mg mL-1, indicating that it has favorable aggregation behavior.[56] Additionally, this blend also exhibits smooth and uniform surfaces (RMS = 1.61 nm, **Figure S13**), which is the lowest value among these blends fabricated with various solution concentrations (**Figure 2D**). These results indicate that an appropriate concentration gradient is conducive to the molecular crystallization of the active layer system in a high-speed printing process. To emphasize the general applicability of this SCTGC strategy, we extended this strategy to other high-performance photovoltaic systems (PM6:L8-BO and DP3:BTP-eC9, see Figure S14A). The corresponding photovoltaic performance parameters of these two systems fabricated by various processing conditions are shown in Figures S14-S16 and Tables S4-S5. As depicted in Figure S14B, the relevant results strongly demonstrate the universality of the SCTGC strategy.[57, 58]

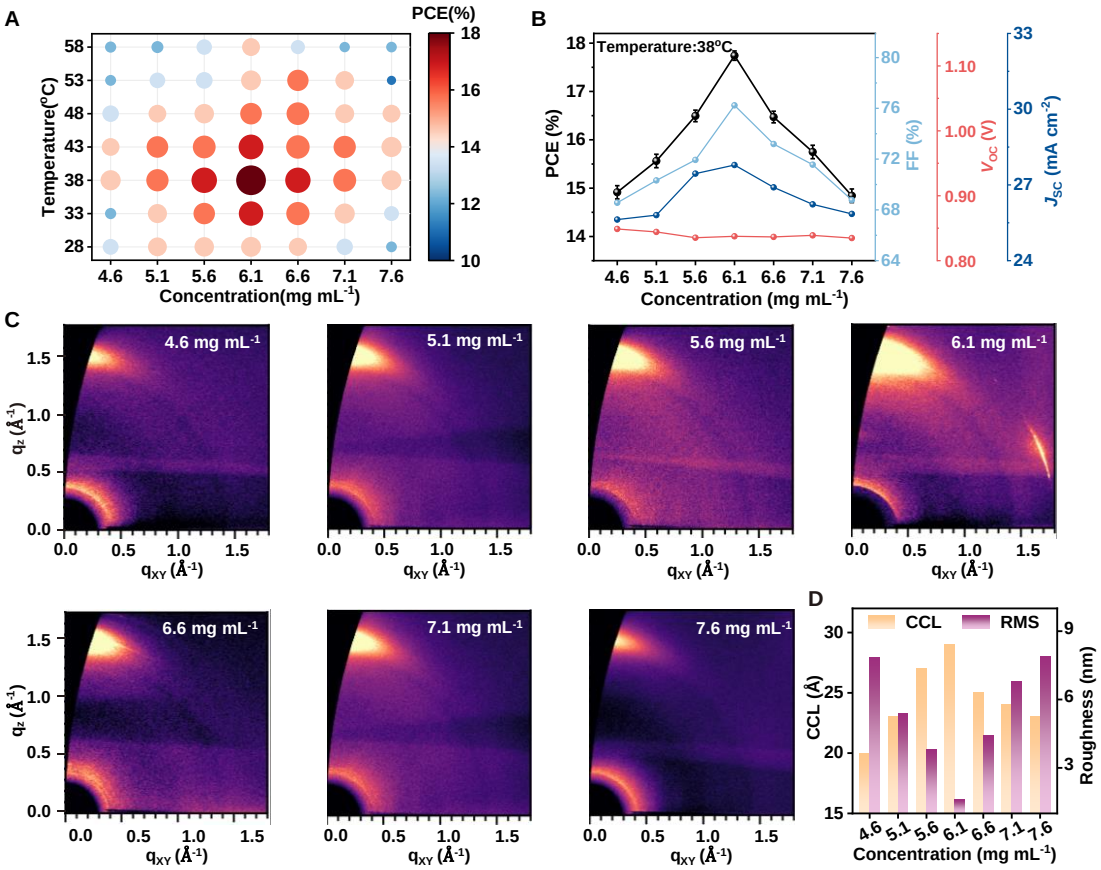

Figure 2. (A) PCE of the PM6/BTP-eC9 LbL devices as a function of solution concentration and baseplate temperature for the top layer. (B) The PCE, V_{OC}, J_{SC}, and FF values of the PM6/BTP-eC9 LbL devices fabricated with different solution concentrations when the baseplate temperature was 38 °C. (C) Two-dimensional GIWAXS patterns of the high-speed coated PM6/BTP-eC9 LbL blends fabricated with different solution concentrations. (D) Corresponding CCL and RMS values of the abovementioned blends.

Furthermore, we investigated the other three normally used solvents to test the suitability for solvent engineering, including chlorobenzene (CB), o-xylene, and toluene. The molecular structures of relevant solvents are exhibited in **Figure 3A**, and the corresponding PCE as a function of concentration and temperature are illustrated in **Figures 3B-D**. Relevant *J-V* curves of the optimized devices fabricated by CB, o-Xylene, and toluene are provided in **Figures S17-S19**, and the related performance parameters are summarized in **Tables S6-S8**. After balancing the substrate temperature and solution concentration, the high performance under these optimized LbL devices fabricated by CB, o-Xylene and toluene are achieved with promising PCEs of 17.19%

(the substrate temperature is 89 °C and the solution concentration is 6.1 mg mL^{-1}), 17.56% (the substrate temperature is 82 °C and the solution concentration is 6.6 mg mL^{-1}), and 17.66% (the substrate temperature is 65 °C and the solution concentration is 6.6 mg mL^{-1}), respectively, which are comparable to those of the corresponding CF-processed LbL devices (PCE = 17.74%; the substrate temperature is 38 °C and the solution concentration is 6.1 mg mL^{-1}). All these results strongly demonstrate the feasibility of employing this synergistic control strategy to improve the solution processability of high-speed fabricated LbL devices.

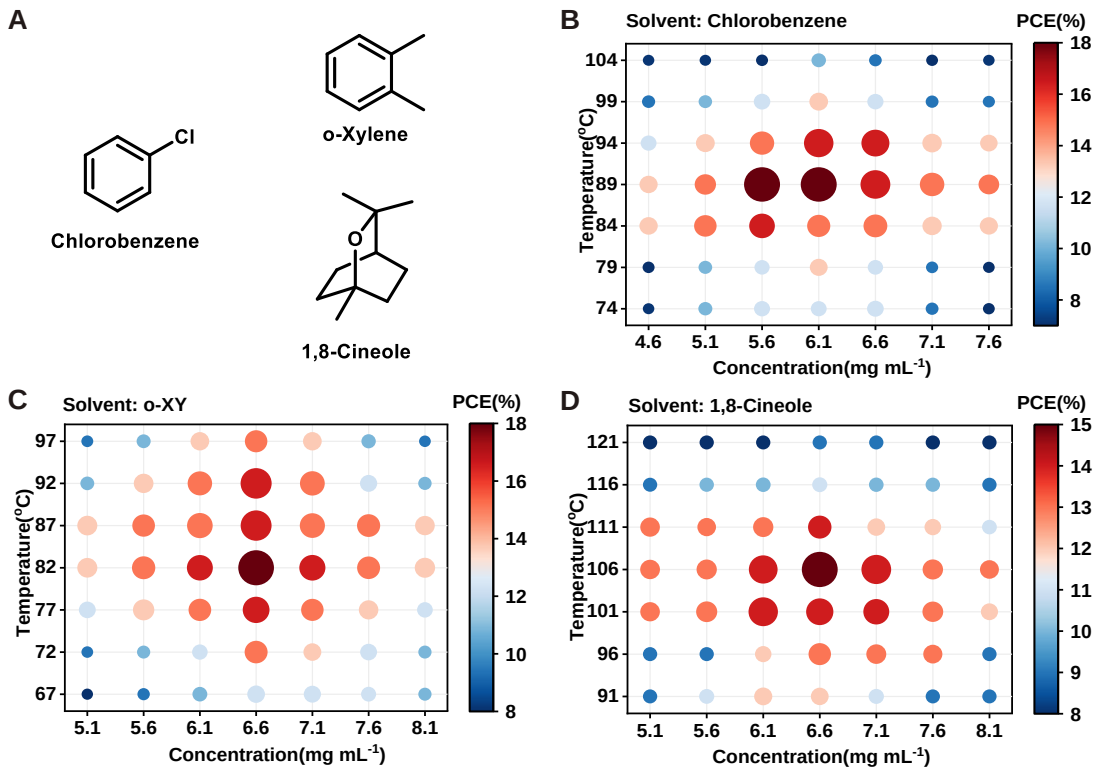

Figure 3. (A) chemical structure of solvents; PCE distribution of the PM6/BTP-eC9 LbL devices fabricated by (B) chlorobenzene, (C) o-Xylene, or (D) toluene. The concentration values in the figure represent the concentrations of both the donor and acceptor solutions.

To further understand the film formation processes of the blends fabricated with various solution concentrations in detail and confirm the direction and force of Marangoni flow (**Figure 4A**), we analyzed the dependence of surface tension on the solution concentration, measured by the dynamic pendant drop method as depicted in **Figure 4B**.[59] The dynamic evolution of droplets' surface tension and volume in real-time was

plotted frame by frame, as exhibited in **Figure S20**. The concentration-dependent surface tensions of the solutions are exhibited in **Figure S21**. Note that the platform's value at the curve's tail can be regarded as the surface tension of the contact line, which can be utilized to compare the concentration gradient in the film formation process of different solutions. It indicates that the surface tension of dilute solutions can be treated as exponential decay, while the variation of concentrated solutions' surface tension changes relatively stable, which might be associated with viscous contact and entanglement of the polymer chain.

For a binary mixture wet film (**Figure 4A**), the Navier-stokes equation can be simplified and the surface velocity, and fluid velocity field at the edge of the wet film can be expressed as:[60]

$$u(r.t) = \underbrace{\frac{\gamma h^2}{2\mu}\left(\frac{\partial p}{\partial r}\right)}_{Capillary flow} + \overbrace{\frac{h}{\mu}\left(\frac{\partial \gamma}{\partial r}\right)}^{Marangoni flow} \quad at\ z = h(r,t)$$

Where the first term in the formula represents the velocity driven by capillary flow, which driven by capillary forces, which arise from a dramatic concentration gradient from the saturation solution to the bulk density of the solute. The second one means the counterpart from Marangoni flow, which originates from the inhomogeneity of solution surface tension-the solution of the wet film surface pulled from the low surface tension region to the high surface tension region. γ is the surface tension of the solvent, μ is the viscosity of the solution, which affects the power of flow equally, and h is a geometric dimension related to the blade gap. $\frac{\partial p}{\partial r}$ is the pressure gradient that Linear correlation with the concentration gradient, $\frac{\partial \gamma}{\partial r}$ is the surface tension gradient, which shows sensitivity to the variation of the concentration gradient and can be treated as the exponential attenuation.[61] For maintaining optimal thickness, dilute solutions are usually used for high-speed coating, thus, in the corresponding film formation process, the power of Marangoni flow can be immediately controlled by adjusting the solution

concentration, while the capillary flow is relatively stable. Based on this analysis, we propose the whole film formation process at different concentration gradients. For the dilute solution (**Figure 4A**), an excessive concentration gradient leads to stronger Marangoni flow than capillary flow, which also means redundant backflow on the air-liquid area. The contact line is under mass transport shortage, causing intermittent solid film growth. Consequently, the film thickness might be stable macroscopically, but local aggregation is also inevitable. This film-formation phenomenon is the so-called 'orange peel effect'. However, the status of the concentrated solution is contrary. The exponential decay Marangoni flow is suppressed by the stable capillary flow, resulting in unconstrained mass transfer to the substrate edge, in other words, the 'coffee ring effect', the consequence of which is an even uniform central area and the obvious thickness between the edge and central area. For optimal concentration gradient, both capillary flow and Marangoni flow are balanced with counterbalance, leading to a stable mass transport process.[17, 62] To further verify the change in film uniformity and homogeneity, the variance of film thickness and surface roughness was measured for blends fabricated at different solution concentrations. The results, as exhibited in **Figure 4C** and **Table S2**, can demonstrate the description and analysis above appropriately.

To investigate the influence of substrate temperature on the film formation process of the high-speed coated blends, we employed *in-situ* UV-Vis absorption spectrum technique to investigate their blends fabricated under the substrate temperatures of 28 ℃, 38 ℃, and 58 ℃, respectively. Here we plot the *in-situ* UV-Vis spectrum (**Figure S22**) of the high-speed coated blends fabricated with a solution concentration of 6.1 mg mL^{-1} under various substance temperatures and further converted these spectra into two-dimensional contour maps (**Figure 4D**). Again, the film formation process can be divided into three different stages as mentioned above.[17, 46] Stage II can be observed with a dramatic red shift in the 2D contour map. For the 28 ℃ conditions (**Figure 4D**), the extraordinarily long evaporation stage lasts until 2.2 s contributing to a low-temperature gradient, then both the donor peak and acceptor peak exhibit a redshift of

0.5 s, corresponding to nucleation and crystallization growth stage. Notably, the intensity of the acceptor peak in **Figure 4G** shows a clear decline trend even before the beginning of the crystallization stage, suggesting that excessive evaporation stage results in early onset of the acceptor's nucleation and adverse effect on optimal morphology. At 38 ℃ (**Figures 4E and 4H**), the lengths of the evaporation stage and crystallization stage are 1 s and 1.6 s, respectively. The balanced temperature gradient facilitates synchronous crystallization of the donor and acceptor, as a result, the peak distribution width has almost doubled, suggesting a more disordered but close stacking of donors, which can contribute to the unique vertical phase structure.[55] Regardless of spectrum and peaks' revolution in **Figure 4F** at 58 ℃ are similar to 38 ℃, the evaporation rate dramatically increased with a high-temperature gradient (**Figure 4I**), which obstructs the spread of homogeneous wet film and stable mass transport process. Moreover, we conducted an in-situ PL test, and the results confirmed the same film-forming process, as shown in **Figure S23**. The corresponding AFM figures of the blend films fabricated under different coating temperatures are shown in **Figures S24A-G**, the lowest thickness roughness value (1.640 nm) was achieved when the substrate temperature was 38℃. This result suggests uniform film can be fabricated at optimal coating temperature. Then we also used TPC and TPV technologies to investigate the effect of the coating temperature on carrier dynamics, as shown in **Figures S24H-I**. The related active layer system fabricated by the optimal coating temperature exhibited a lower current extraction time and a higher carrier lifetime in devices as compared to the related systems fabricated by other coating temperatures

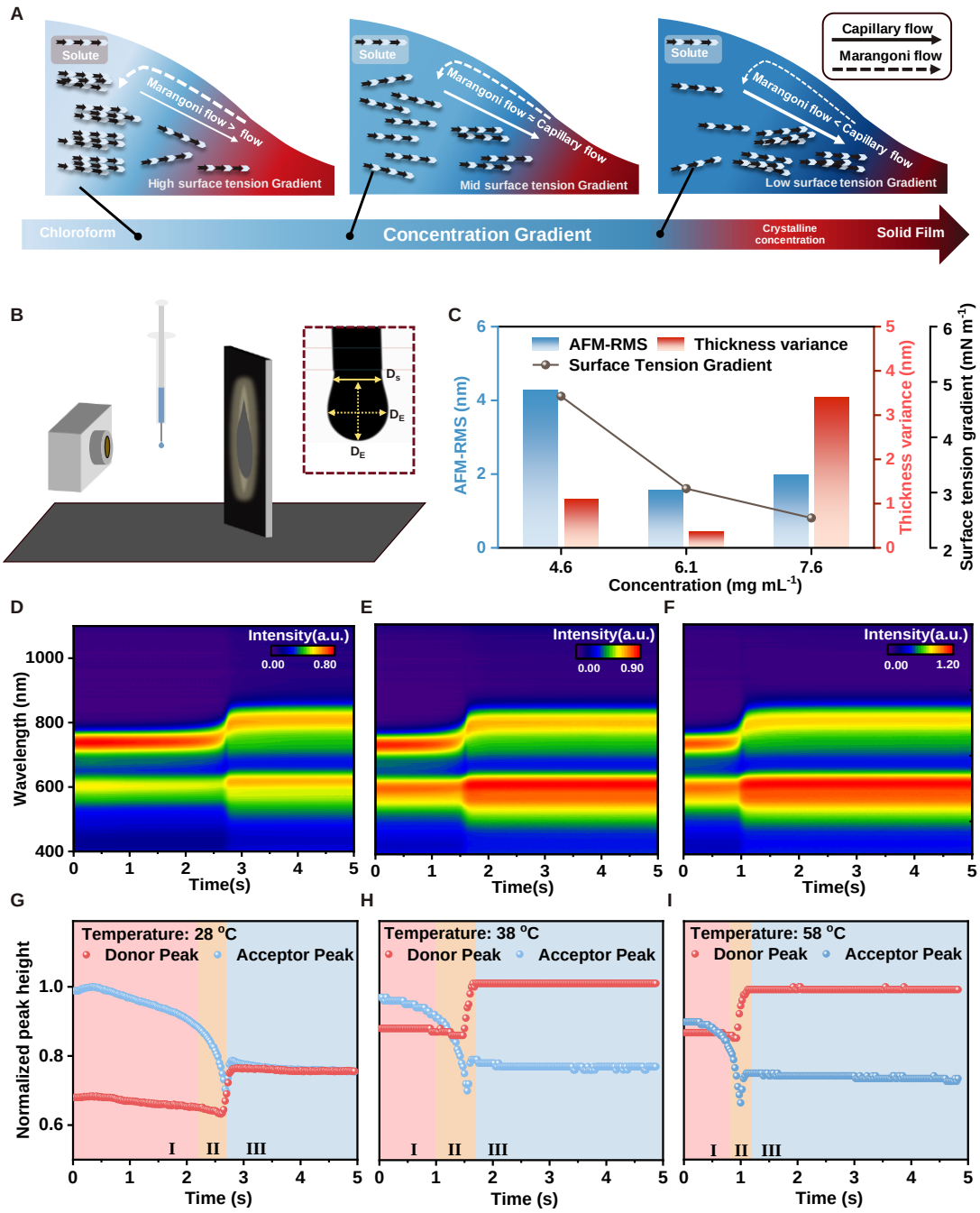

Figure 4. (A) The evolution of capillary flow and Marangoni flow in the film formation process driven by the different concentration gradients. (B) The test platform of surface tension. (C) The surface tension, surface roughness, and thickness variance of blends fabricated at different concentrations. Colorful scan spectrum of devices fabricated under (D) 28℃ (E) 38℃ and (F) 58℃. Peak intensity evolution curves of donor and acceptor peaks of the high-speed coated blend, fabricated under (G) 28℃ (H) 38℃ and (I) 58℃.

In this work, our results demonstrate that the choice of processing conditions (e.g. substrate temperature and solution concentration) enables changing the molecular

ordering and fine-tuning the nanoscale phase separation. This, in turn, is likely to cause changes in the film formation processes (**Figure 4**), fundamental photo-physical processes, and device performance (**Figure 2**). Based on the above analysis, the synergistic effect between concentration-temperature gradient can be regarded as a combination of mass-transport process control and crystallization process control, as illustrated in **Figure 5**. On the one hand, the change in solution concentration can fine-tune the balance between Marangoni flow and capillary flow in the film formation process, which determines the thickness distribution and film quality. Low solution concentration led to stronger reflux and excessive concentration at the midline, while high solution concentration resulted in mass accumulation at the edge. On the other hand, for the substrate temperature, a suitable temperature gradient can scale the time of the first two stages in the crystallization process efficiently, which provides just enough time for the microflow. Low temperature means unexpected donor aggregation during re-dissolution, and high temperature can result in too-fast evaporation of solution and unbalanced mass transport. The coordinated regulation of these two processing conditions is critical to improving the high-speed solution processability of the specific active layer system.

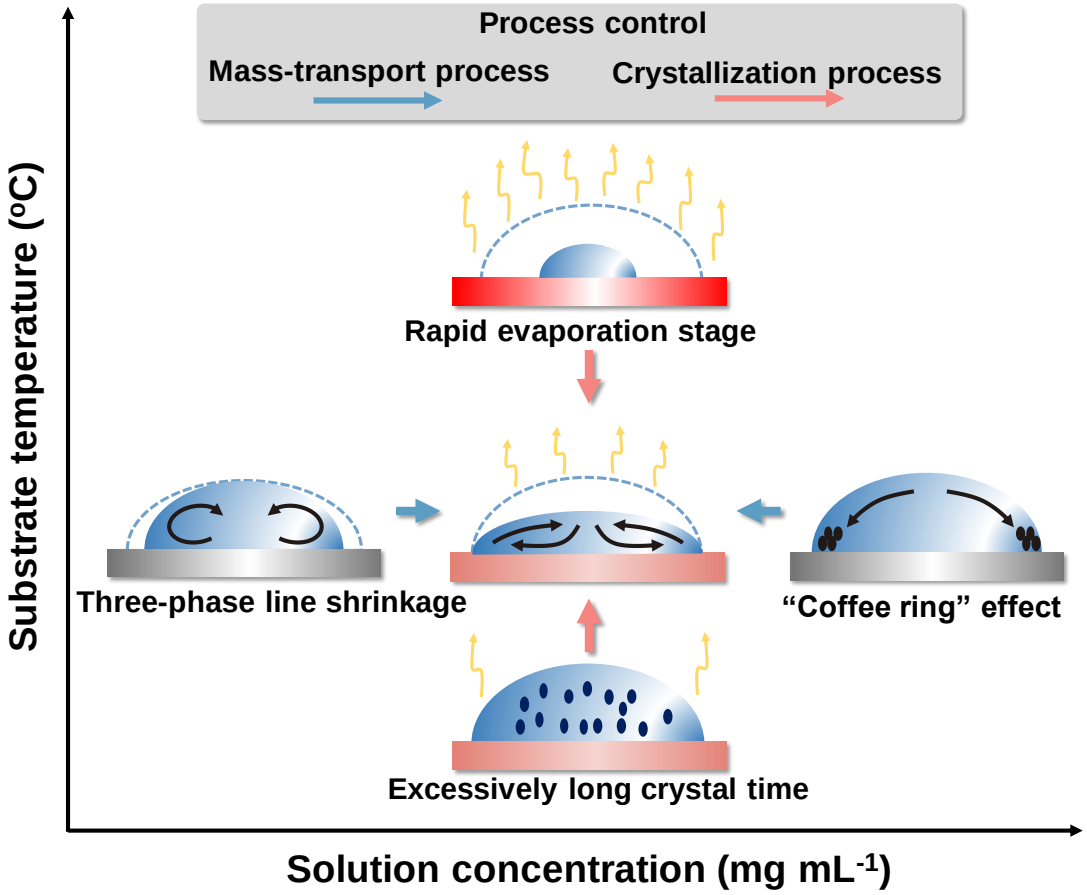

Figure 5. The evolution of morphological characteristics and high-speed print film formation processes as a function of solution concentration and substrate temperature.

Conclusion

The high-throughput compatibility of the active layer fabrication needs to be reconsidered, owing to the differences in film-formation dynamics between the low-speed process and high-speed coating process,[22] supported by our analysis (**Figure 1**). Impressively, we found that the high-speed coating processability of OPV systems can be achieved by synergistically adjusting the substrate temperature and solution concentration during the deposition of the donor and acceptor layers. Using the LbL processing strategy and the SCTGC method, we successfully constructed the high-performance PM6: BTP-eC9 devices fabricated at high coating speeds with both halogenated solvents and non-halogenated solvents, including CF, CB, o-xylene, and toluene. Taking CF as an example, An in-depth study of microstructure variations and

physical mechanisms based on the films processed under identical baseplate temperatures and various solution concentration were performed by multi-scale morphological characterization techniques and multi-photoelectric process to investigate differences in device performance with respective to fundamental photo-physical processes in parallel and confirm the optimization effect of this SCTGC strategy. Furthermore, solution microfluidics analysis and in-situ UV-vis spectrum monitor were employed to depict the whole active layer formation process, from the deposition of wet film to solid film formation, which indicates that the effect of the solution concentration gradient and temperature gradient are embodied in the mass-transport control and crystallization process control, respectively. This work introduces an efficient SCTGC strategy to obtain a high-speed coated active layer with high performance, while unraveling the whole film formation process in the high-speed coating, thus opening a new view for decreasing the lab-to-fab PCE loss for the scalable fabrication of OPV.

Supporting Information

Supporting Information is available from…...

Acknowledgments

This work was financially supported by the National Natural Science Foundation of China (NSFC) (Grant No. 22279094 and 223B2904), Hubei Provincial Natural Science Foundation (2024AFB068) and the Fundamental Research Funds for the Central Universities. This work was supported by the Open Fund of the State Key Laboratory of Luminescent Materials and Devices (South China University of Technology, 2024-skllmd-23) and the opening project of the Key Laboratory of Advanced Electrode Materials for Novel Solar Cells for the Petroleum and Chemical Industry of China (2024A051). We thank the beamline BL14 at Shanghai Synchrotron Radiation Facility (China) for providing the beam time and help during the experiment and thank the Core Facility of Wuhan University for the AFM measurements.

Author Contributions

B. Xiao, R. Sun, and J. Min conceived the ideas. B. Xiao and R. S. fabricated the solar cell samples, conducted the measurements, and performed data analysis. W. Wu conducted the TPC and TPV measurements. S. Wang conducted the AFM measurement. J. Wan assisted in completing the in-situ Abs measurements. Y. Shao provided the DP3 material. R. Sun, B. Xiao, and J. Min contributed to manuscript preparation. All authors commented on the manuscript.

Conflict of Interest

The authors declare no competing interests.

Keywords

Layer-by-Layer, blade-coating, high-speed, morphology modulation, film-forming process

References

1. C. J. Brabec, A. Distler, X. Du, H. J. Egelhaaf, J. Hauch, T. Heumueller, N. Li, *Adv. Energy Mater.* **2020**, *10*, 2001864.
2. I. Burgués-Ceballos, L. Lucera, P. Tiwana, K. Ocytko, L. W. Tan, S. Kowalski, J. Snow, A. Pron, H. Bürckstümmer, N. Blouin, G. Morse, *Joule* **2021**, *5*, 2261.
3. X. Yang, Y. Shao, S. Wang, M. Chen, B. Xiao, R. Sun, J. Min, *Adv. Mater.* **2023**, 2307863.
4. J. Song, Y. Li, Y. Cai, R. Zhang, S. Wang, J. Xin, L. Han, D. Wei, W. Ma, F. Gao, Y. Sun, *Matter* **2022**, *5*, 4047.
5. J. Yi, G. Zhang, H. Yu, H. Yan, *Nat. Rev. Mater.* **2023**, *9*, 46.
6. Y. Gao, B. Xiao, S. Wang, M. Chen, W. Wang, X. Yang, Y. Shao, R. Sun, J. Min, *Sci. China Chem.* **2023**, *66*, 3205.

7. R. Sun, Y. Wu, X. Yang, Y. Gao, Z. Chen, K. Li, J. Qiao, T. Wang, J. Guo, C. Liu, X. Hao, H. Zhu, J. Min, *Adv. Mater.* **2022**, *34*, 2110147.

8. L. Zhu, M. Zhang, J. Xu, C. Li, J. Yan, G. Zhou, W. Zhong, T. Hao, J. Song, X. Xue, Z. Zhou, R. Zeng, H. Zhu, C. C. Chen, R. C. I. MacKenzie, Y. Zou, J. Nelson, Y. Zhang, Y. Sun, F. Liu, *Nat. Mater.* **2022**, *21*, 656.

9. X. Kong, L. Zhan, Z. Li, Y. Yang, Y. Liu, H. Qiu, X. Sun, H. Hu, R. Sun, J. Min, S. Yin, W. Fu, H. Chen, *Aggregate* **2024,** 553.

10. P. Bi, J. Wang, Y. Cui, J. Zhang, T. Zhang, Z. Chen, J. Qiao, J. Dai, S. Zhang, X. Hao, Z. Wei, J. Hou, *Adv. Mater.* **2023**, *35*, 2210865.

11. S. Guan, Y. Li, C. Xu, N. Yin, C. Xu, C. Wang, M. Wang, Y. Xu, Q. Chen, D. Wang, L. Zuo, H. Chen, *Adv. Mater.* **2024**, *36*, 2400342.

12. J. Wang, Y. Wang, J. Li, Y. Yu, P. Bi, J. Qiao, Z. Chen, C. Wang, W. Wang, J. Dai, X. Hao, S. Zhang, J. Hou, *Angew. Chem. Int. Ed.* **2023**, *62*, 202314362.

13. R. Sun, W. Wang, H. Yu, Z. Chen, X. Xia, H. Shen, J. Guo, M. Shi, Y. Zheng, Y. Wu, W. Yang, T. Wang, Q. Wu, Y. Yang, X. Lu, J. Xia, C. J. Brabec, H. Yan, Y. Li, J. Min, *Joule* **2021**, *5*, 1548.

14. P. Ding, D. Yang, S. Yang, Z. Ge, *Chem. Soc. Rev.* **2024**, *53*, 2350.

15. H. Xu, J. Han, S. Chen, Y. Liu, L. Huerta Hernandez, J. Bertrandie, M. Babics, S. Alam, D. R. Villalva, S. H. K. Paleti, J. Gorenflot, C. Herok, N. Ramos, J. Troughton, A. Sharma, T. B. Marder, B. Engels, J. Martin, S. De Wolf, F. Laquai, D. Baran, *Joule* **2023**, *7*, 2135.

16. J. Guo, J. Min, *Adv. Energy Mater.* **2018**, *9*, 1802521.

17. H. Chen, R. Zhang, X. Chen, G. Zeng, L. Kobera, S. Abbrent, B. Zhang, W. Chen, G. Xu, J. Oh, S.-H. Kang, S. Chen, C. Yang, J. Brus, J. Hou, F. Gao, Y. Li, Y. Li, *Nat. Energy* **2021**, *6*, 1045.

18. R. Sun, T. Wang, Z. Luo, Z. Hu, F. Huang, C. Yang, J. Min, *Sol. RRL* **2020**, *4*, 2000156.

19. Y. Shao, R. Sun, W. Wang, X. Yang, C. Sun, Y. Li, J. Min, *Sci. China Chem.* **2023**, *66*, 1101.

20. Q. Wu, J. Guo, R. Sun, J. Guo, S. Jia, Y. Li, J. Wang, J. Min, *Nano Energy* **2019**, *61*, 559.

21. X. Gu, L. Shaw, K. Gu, M. F. Toney, Z. Bao, *Nat. Commun.* **2018**, *9*, 534.

22. T. W. R. Sun, X. Yang, Y. Wu, Y. Wang, M Zhang, C. J. Brabec, Y. Li, Q. Wu,J. Min, *Nat. Energy* **2022,** *7*, 1087.

23. R. Sun, J. Guo, C. Sun, T. Wang, Z. Luo, Z. Zhang, X. Jiao, W. Tang, C. Yang, Y. Li, J. Min, *Energy Environ. Sci.* **2019**, *12*, 384.

24. H. Tian, Y. Ni, W. Zhang, Y. Xu, B. Zheng, S. Y. Jeong, S. Wu, Z. Ma, X. Du, X. Hao, H. Y. Woo, L. Huo, X. Ma and F. Zhang, *Energy Environ. Sci.*, **2024**, *17*, 5173.

25. H. Zhang, Y. Liu, G. Ran, H. Li, W. Zhang, P. Cheng, Z. Bo, *Adv. Mater.* **2024**, *36*, 2400521.

26. C. Xie, X. Zeng, C. Li, X. Sun, S. Liang, H. Huang, B. Deng, X. Wen, G. Zhang, P. You, *Energy Environ. Sci.* **2024**, *17*, 2441.

27. W. Wu, Y. Luo, T. A. Dela Peña, J. Yao, M. Qammar, M. Li, H. Yan, J. Wu, R. Ma, G. Li, *Adv. Energy Mater.* **2024**, *14*, 2400354.

28. L. Wang, C. Chen, Y. Fu, C. Guo, D. Li, J. Cheng, W. Sun, Z. Gan, Y. Sun and B. Zhou, *Nat. Energy* **2024**, *1*, 11.

29. X. Chen, Y. Li, W. Jing, T. Zhou, X. Xu, Y. Duan, L. Yu, R. Li and Q. Peng, *Angew. Chem. Int. Ed.* **2024**, *63*, 202402831.

30. W. Xu, H. Tian, Y. Ni, Y. Xu, L. Zhang, F. Zhang, S. Wu, S. Young Jeong, T. Huang, X. Du, X. Li, Z. Ma, H. Young Woo, J. Zhang, X. Ma, J. Wang and F. Zhang, *Chem. Eng. J.* **2024**, *493*, 152558.

31. R. Sun, Q. Wu, J. Guo, T. Wang, Y. Wu, B. Qiu, Z. Luo, W. Yang, Z. Hu, J. Guo, M. Shi, C. Yang, F. Huang, Y. Li, J. Min, *Joule* **2020**, *4*, 407.

32. J. G, J. Min, *Adv. Energy Mater.* **2019**, *9*, 1802521.

33. Y. F. Liu, A. Yangui, R. Zhang, A. Kiligaridis, E. Moons, F. Gao, O. Inganäs, I. G. Scheblykin, F. L. Zhang, *Small Methods* **2021**, *5*, 2100585.

34. M. Kasischke, S. Hartmann, K. Niermann, M. Smarra, D. Kostyrin, U. Thiele, E. L. Gurevich, *Phys. fluids* **2023**, *35*, 074117.

35. X. Zhao, R. Sun, X. Wu, M. Zhang, Y. Gao, J. Wan, J. Min, *Energ. Environ. Sci.* **2023**, *16*, 1711.

36. G. Park, Y. Cho, S. Jeong, J. Park, S.-J. Yoon, C. Yang, *J. Mater. Chem. A* **2023**, *11*, 12185.

37. F. Gumpert, A. Janßen, C. J. Brabec, H.-J. Egelhaaf, J. Lohbreier, A. Distler, *Eng. Appl. Comput. Fluid Mech.* **2023**, *17*, 1.

38. J. E. Carlé, M. Helgesen, O. Hagemann, M. Hösel, I. M. Heckler, E. Bundgaard, S. A. Gevorgyan, R. R. Søndergaard, M. Jørgensen, R. García-Valverde, S. Chaouki-Almagro, J. A. Villarejo, F. C. Krebs, *Joule* **2017**, *1*, 274.

39. Y. Gao, B. Xiao, S. Wang, M. Chen, W. Wang, X. Yang, Y. Shao, R. Sun, J. Min, *Sci. China Chem.* **2023**, *66*, 3205.

40. L.Y. Xu, Y. Gao, W. Wang, Y. Shao, M. Chen, X. Yang, Y. Fu, M. Zhang, X. Lu, R. Sun, J. Min, *Energy Environ. Sci.* **2023**, *16*, 3942-3950.

41. H. Zhou, C. Liu, S. Liu, Z. Zhang, S. Sun, W. Xu, X. Ma, J. Wang, Y. Xu, X. Du, *Small* **2024**, *20*, 2308216.

42. X. Yang, R. Sun, Y. Wang, M. Chen, X. Xia, X. Lu, G. Lu, J. Min, *Adv. Mater.* **2023**, *35*, 2209350.

43. X. Xu, Y. Li, Q. Peng, *Adv. Mater.* **2022**, *34*, 2107476.

44. X. Zhao, R. Sun, X. Wu, M. Zhang, Y. Gao, J. Wan, J. Min, *Energy Environ. Sci.* **2023**, *16*, 1711.

45. L. Zhan, S. Li, X. Xia, Y. Li, X. Lu, L. Zuo, M. Shi, H. Chen, *Adv. Mater.* **2021**, *33*, 2007231.

46. X. Zhao, R. Sun, X. Wu, M. Zhang, Y. Gao, J. Wan and J. Min, *Energy & Environmental Science*, 2023, **16**, 1711-1720.

47. R. Sun, Q. Wu, J. Guo, T. Wang, Y. Wu, B. Qiu, Z. Luo, W. Yang, Z. Hu, J. Guo, M. Shi, C. Yang, F. Huang, Y. Li, J. Min, *Joule* **2020**, *4*, 407.

48. J. Xue, H. Zhao, B. Lin, Y. Wang, Q. Zhu, G. Lu, B. Wu, Z. Bi, X. Zhou, C. Zhao, *Adv. Mater.* **2022**, *34*, 2202659.

49. X. Jiang, P. Chotard, K. Luo, F. Eckmann, S. Tu, M. A. Reus, S. Yin, J. Reitenbach, C. L. Weindl, M. Schwartzkopf, *Adv. Energy Mater.* **2022**, *12*, 2103977.

50. H. Yu, Y. Wang, X. Zou, J. Yin, X. Shi, Y. Li, H. Zhao, L. Wang, H. M. Ng, B. Zou, X. Lu, K. S. Wong, W. Ma, Z. Zhu, H. Yan, S. Chen, *Nat. Commun.* **2023**, *14*, 2323.

51. Y. Liang, D. Zhang, Z. Wu, T. Jia, L. Lüer, H. Tang, L. Hong, J. Zhang, K. Zhang, C. J. Brabec, N. Li, F. Huang, *Nat. Energy* **2022**, *7*, 1180.

52. Y. Wu, J. Guo, W. Wang, Z. Chen, Z. Chen, R. Sun, Q. Wu, T. Wang, X. Hao, H. Zhu, J. Min, *Joule* **2021**, *5*, 1800.

53. S. Wang, L.-Y. Xu, B. Xiao, M. Chen, M. Zhang, W. Gao, B. Xiao, A. K. Y. Jen, R. Yang, J. Min, R. Sun, *Energy Environ. Sci.* **2024**, *17*, 2610.

54. L. Zhang, R. Sun, Z. Zhang, J. Zhang, Q. Zhu, W. Ma, J. Min, Z. Wei, D. Deng, *Adv. Mater.* **2022**, *34*, 2207020.

55. Y. Zheng, R. Sun, M. Zhang, Z. Chen, Z. Peng, Q. Wu, X. Yuan, Y. Yu, T. Wang, Y. Wu, X. Hao, G. Lu, H. Ade, J. Min, *Adv. Energy Mater.* **2021**, *11*, 2102135.

56. C. Sun, F. Pan, H. Bin, J. Zhang, L. Xue, B. Qiu, Z. Wei, Z. G. Zhang, Y. Li, *Nat. Commun.* **2018**, *9*, 743.

57. Y. Shao, Y. Gao, R. Sun, M. Zhang and J. Min, *Adv. Mater.* **2023**, *35*, 2208750.

58. C. Li, J. Zhou, J. Song, J. Xu, H. Zhang, X. Zhang, J. Guo, L. Zhu, D. Wei, G. Han, J. Min, Y. Zhang, Z. Xie, Y. Yi, H. Yan, F. Gao, F. Liu and Y. Sun, *Nat. Energy* **2021**, *6*, 605.

59. N. Bagalkot, A. A. Hamouda, O. M. Isdahl, *MethodsX* **2018**, *5*, 676.

60. H. Kim, F. Boulogne, E. Um, I. Jacobi, E. Button, H. A. Stone, *Phys. Rev. Lett.* **2016**, *116*, 124501.

61. Z. Liu, Z. Li, Z. Cai, Y. Qiao, Y. Yang, S. Chen, X. Ma, H. Li, Q. Meng, F. Zhang, Y. Song, J. Mater. Chem. C **2021**, *9*, 17518.

62. G. Shi, Z. Huang, R. Qiao, W. Chen, Z. Li, Y. Li, K. Mu, T. Si, Z. Xiao, *Nat. Commun.* **2024**, *15*, 1066.